nature communications

Article

https://doi.org/10.1038/s41467-025-64607-4

Three stages of plateau evolution manifested in present-day Tibetan Plateau

Received: 15 July 2024

Accepted: 18 September 2025

Published online: 30 October 2025

Check for updates

Shihua Cheng[1], Xiao Xiao[1], Li Sun[2], Weilai Wang[3], Jianping Wu[3], Xiaoxin Wang[1,2], Xiaofeng Liang[4], Xiaobo Tian[4], Hongyi Li[5] & Lianxing Wen[6]

Notwithstanding the evolution of the Tibetan Plateau being a fundamental topic in continental dynamics, general mechanisms of Plateau uplift remain elusive and past Plateau evolution models lack clarity of the actual geodynamical process. Here, with detailed mappings of intra-crustal low-velocity zones and crust-mantle discontinuity in the region using the seismic data consolidated by the China Seismological Reference Model project, we show that the present-day Tibetan Plateau manifests three stages of mid-crustal flow driven evolution that can be clearly identified in three distinct regions of the Plateau: a pre-response stage with a young mid-crustal partially molten zone but little response of surface topography and crust-mantle discontinuity, the first stage with a mature mid-crustal partially molten zone by deepening crust-mantle discontinuity without large-scale surface uplift, and the last stage by large-scale surface uplifting. Our results provide direct observation and a unique reference of geodynamical responses at different evolution stages of the continent-continent collision zones.

Many evolution models of the Tibetan Plateau (the Plateau) have been proposed, with general dynamical mechanisms ranging from continuous shortening and thickening of the Plateau[1,2], rigid block extrusion[3–5] to mid-crustal flow[6–10], and evolution history being multiple-phase uplifting[5,11–14]. Yet, those general mechanisms remain controversial and the proposed multiple-phase uplifting models lack clarity of the actual geodynamical process.

The above studies demonstrated the importance of exploring geological history and geodynamical modelling in advancing our knowledge about the Plateau evolution. However, it is possible that different regions of the present-day Plateau may be at different stages of continental plateau evolution and identifying those stages in the present-day Plateau provides a straightforward way to decipher the physical mechanism of the Plateau formation and geodynamical responses at different evolution stages of the Plateau. In particular, the spatial distribution and structural features of intra-crustal low-velocity zones (LVZs) would provide insights into the most plausible mechanisms of the Plateau evolution, while the relationship between LVZs, surface topography and the depth of the crust-mantle discontinuity (the Moho discontinuity) could provide crucial information in identifying regions at different stages of the Plateau evolution. Such an approach, however, is hindered by the unclear picture of LVZ features in the region and the poor resolution of the spatial variation of the Moho depth. The existence of LVZs was well established in different parts of the Plateau in many seismological studies[15–22], but it remains unclear what geographic extent the LVZs exist in, what the detailed features of LVZs are and how the LVZ features vary within the Plateau. The existence of low-resistance zones in the middle-to-lower crust, likely associated with the LVZs reported in the seismological studies, was also reported in some magnetotelluric studies beneath some

[1]Laboratory of Seismology and Physics of Earth's Interior, School of Earth and Space Sciences, University of Science and Technology of China, Hefei, China. [2]China Earthquake Networks Center, China Earthquake Administration, Beijing, China. [3]Institute of Geophysics, China Earthquake Administration, Beijing, China. [4]State Key Laboratory of Lithospheric Evolution, Institute of Geology and Geophysics, Chinese Academy of Sciences, Beijing, China. [5]State Key Laboratory of Geological Processes and Mineral Resources, School of Geophysics and Information Technology, China University of Geosciences, Beijing, China. [6]Department of Geosciences, State University of New York at Stony Brook, Stony Brook, NY, USA. e-mail: lianxing.wen@stonybrook.edu

regions of the Plateau (Fig. 1a and Supplementary Table 1), but the studied regions remain limited and the geometry and boundary properties of those low-resistance zones cannot be clearly defined due to the nature of magnetotelluric measurements. Similarly, the inferred Moho depth exhibited poor spatial resolutions in the region due to insufficient seismic coverage in the past (Supplementary Table 2). Recent years have witnessed a drastic change of seismic coverage in the region of the Plateau, especially with the launch of a national initiative in China, the China Seismological Reference Model (CSRM) project[23], that has consolidated an unprecedented amount of seismic data in the region.

In this study, we map out detailed geographic distribution and characteristics of intra-crustal LVZs in and around the Plateau through an approach of joint inversion of various seismic constraints derived from the CSRM data. Together with the high-resolution crustal thickness map produced by the CSRM project[23,24], we examine possible stages of continental plateau evolution in the present-day Plateau.

Results

Data and inversion of LVZ features

LVZ features are identified through seismic shear-wave velocity (V_S) profiles inverted using three types of seismic constraints: teleseismic compressional-wave (*P*-wave) receiver functions (RFs) obtained from the seismic data of the teleseismic events, Rayleigh wave phase velocities inferred based on the continuous ambient noise and earthquake data, and vertical/horizontal (ZH) displacement ratios of the Rayleigh wave obtained from the seismic data of the teleseismic events (see Methods section). The RF dataset includes a total of 727,201 RFs extracted from the seismic data of 1933 seismic stations (Fig. 1b). RFs are corrected to have the same reference ray parameter of 0.06 s km^{-1}, bin-stacked over back-azimuth bins with a bin width of 10°, and manually checked to ensure high quality. The bin-stacked RFs are classified into two types based on the visibility of a prominent negative phase (termed here as *Pls* phase for discussion purposes) before the *Pms* phase (*P*-to-*S* conversions at the Moho discontinuity), and are further grouped into back-azimuth clusters based on their waveform similarity and stacked within the clusters yielding the cluster-stacked RFs (Supplementary Fig. 1). The Rayleigh wave phase velocities (Supplementary Fig. 2a) are inverted by a simultaneous inversion method[25], with models in the period range of 8–50 s constrained by both the inter-station measurements from the ambient noise and event-station measurements from local earthquake data and those in the period range of 50–70 s constrained by the event-station measurements (Supplementary Fig. 2, b and c). The ZH ratio dataset is constructed from 4709 seismic event data samples from the region collected for the seismic stations that have high-quality RFs (Fig. 1b and Supplementary Fig. 3).

Crustal V_S profiles are inverted for the sites of each seismic station along each back-azimuth of the cluster-stacked RFs using a Markov Chain Monte Carlo (MCMC) algorithm[26,27], by minimizing the misfit between the three types of seismic observations and the synthetics (see Methods section). Two separate model parametrization schemes are used in accordance with the presence or absence of *Pls* phase in the cluster-stacked RF. For the observations with the cluster-stacked RF exhibiting no *Pls* phase, V_S profile is parameterized with three layers: a shallow sediment, a crystalline crust, and an uppermost mantle; for the observations with the cluster-stacked RF exhibiting a prominent *Pls* phase, an LVZ with a sharp top discontinuity is required to explain the *Pls* phase and is added in the crystalline crust layer. The best-fitting V_S model and its uncertainty are estimated through statistical analysis of the model assemblage selected from 50,000 sampled models in iterations. The best-fitting V_S model is the sampled model nearest to

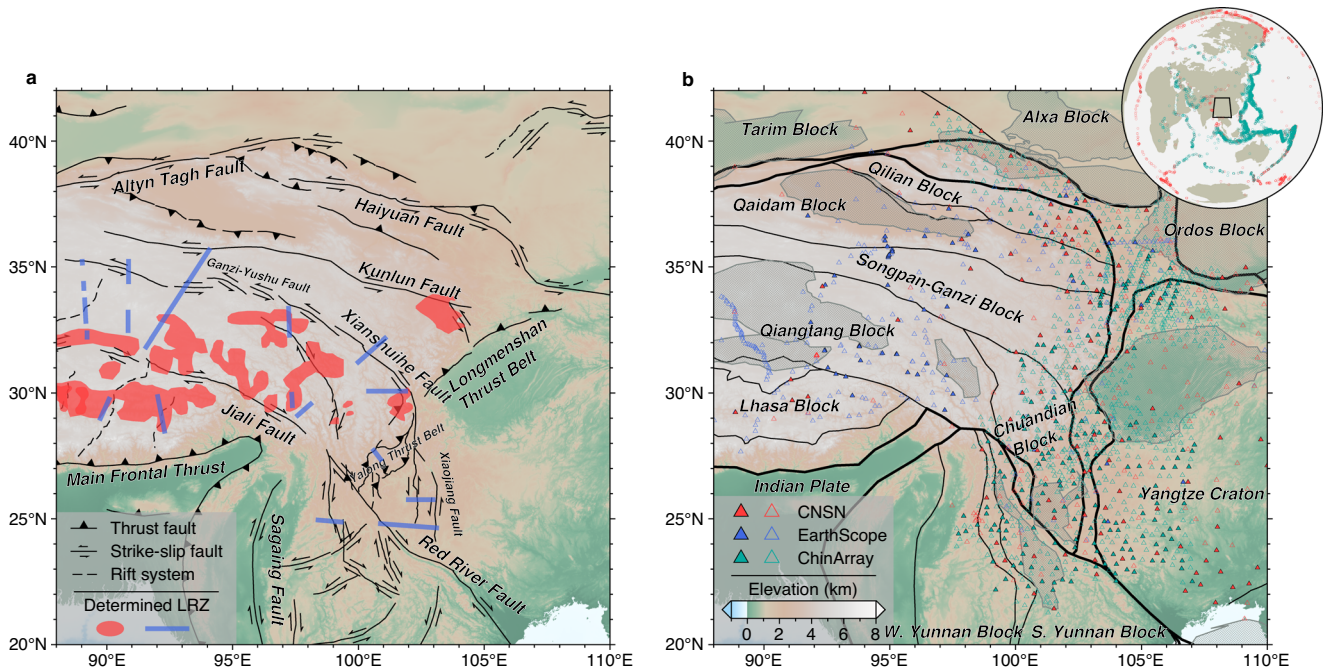

Fig. 1 | Geological and geophysical data in the study region. a Major geological faults (lines, with the names of the faults labelled and data sources from Yin and Harrison[67] and Pitard et al. [49] and low-resistivity zones (LRZs, red-shaded regions for regional mapping results and blue lines for line mapping results) in the middle-to-lower crust determined by magnetotelluric tomography (see Supplementary Table 1 for data source). **b** Tectonic blocks and data sources of seismic stations and seismic events. Seismic stations include 302 permanent stations from the China National Seismic Networks (CNSN) (red triangles), 468 permanent or temporary stations from the EarthScope (blue triangles), and 1163 temporary stations from the China Seismic Array (ChinArray) (cyan triangles). Stations marked with solid triangles are used in this study, while those marked with hollow triangles do not have good data quality and are not used. Geological units and major basins (data sources from Zhang et al. [68] and Shen et al. [60] are denoted by enclosed-black lines and grey-shaded regions, respectively. The inset shows the locations of seismic events (with the event catalogue from the EarthScope) of data sources for receiver functions (cyan circles) and ZH ratios (red circles), with the black box indicating the region of the study. Background in (**a**) and (**b**) is topography from the ETOPO1 (https://doi.org/10.7289/V5C8276M).

https://doi.org/10.1038/s41467-025-64607-4

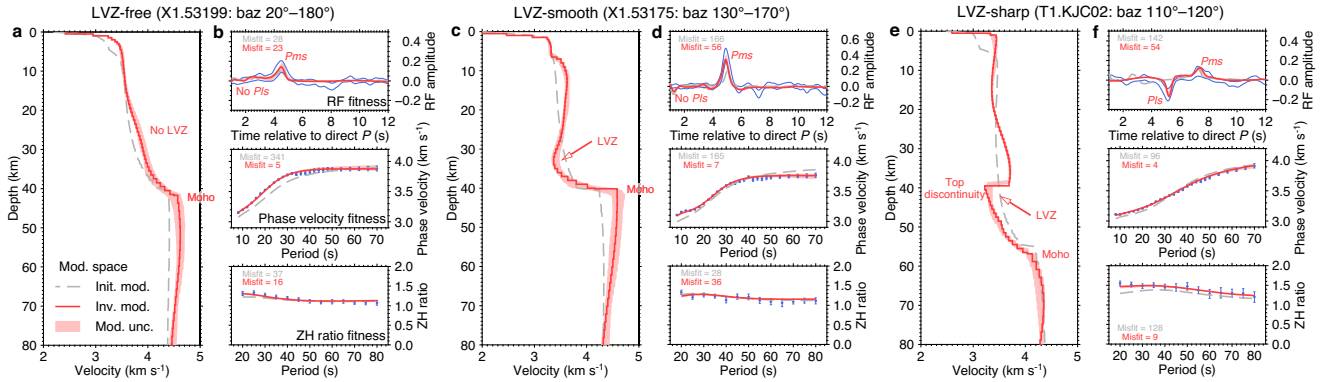

Fig. 2 | Examples of shear-wave velocity (V_S) profile inversion on three sites with different features of low-velocity zone (LVZ) in the crust. For the site of station X1.53199 along the back-azimuth (baz) range from 20° to 180° with a representative "LVZ-free" crustal profile: **a** initial model (labelled as "Init. mod.", grey-dashed curve), inverted model (labelled as "Inv. mod.", red curve) and two standard deviations interval of all acceptable models (labelled as "Mod. unc.", red-shaded area); **b** comparisons of seismic observations and synthetics computed with initial model (grey-dashed curves) and inverted model (red curves) for cluster-stacked receiver function (RF) and phase velocities and vertical/horizontal (ZH) displacement ratios of the Rayleigh wave at different periods. The observed values and uncertainties are marked with the area enclosed by blue curves for cluster-stacked RF and are represented by blue dots and vertical bars, respectively, for phase velocities and ZH ratios at different periods. Two standard deviation intervals of synthetics from all acceptable models are marked with red-shaded areas. Misfits between seismic observations and synthetics are labelled in grey for the initial model and red for the inverted model. **c**, **d** Same as **a**, **b**, except for the site of station X1.53175 along the back-azimuth range from 130° to 170° with a representative "LVZ-smooth" crustal profile. **e**, **f** Same as **a**, **b**, except for the site of station T1.KJC02 along the back-azimuth range from 110° to 120° with a representative "LVZ-sharp" crustal profile. Data misfits of the inverted models are reduced to 11% (X1.53199), 28% (X1.53175) and 18% (T1.KJC02) of those of the initial models. Geographic locations of the three example sites are marked in Fig. 3a.

the average of all acceptable models and the model uncertainty is two standard deviations of all acceptable models. The MCMC joint inversion effectively identifies the existence of the LVZs in the region and constrains the detailed seismic structure around those LVZs, as RFs provide crucial information about the existence and sharpness of the LVZs and dispersion curves of phase velocity and ZH ratio constrain the overall V_S structure at depth. The inverted models yield excellent synthetic fitting to the seismic data (see examples in Fig. 2 and Supplementary Fig. 4). Quantitatively, an LVZ is defined as a localized V_S reduction in a certain depth range with the minimum V_S reaching a value less than 3.47 km s^{-1}.

Presence, absence and features of LVZs

Inverted V_S profiles can be classified into three types based on features of LVZ in the crust: (1) "LVZ-free" with no presence of an LVZ (Fig. 2 and Supplementary Fig. 4, a and b), (2) "LVZ-smooth" with presence of an LVZ and a smooth transitional top boundary (Fig. 2 and Supplementary Fig. 4, c and d), and (3) "LVZ-sharp" with presence of an LVZ and a sharp top velocity discontinuity (Fig. 2 and Supplementary Fig. 4, e and f). All LVZs exhibit low V_S zones with ~76% of their values < 3.40 km s^{-1}, and sharp and smooth LVZs are separately identified unlike previous studies that did not distinguish between them[15–22]. Synthetic tests indicate that the existence and seismic properties of those LVZs are well constrained by the seismic data (Supplementary Note 1 and Supplementary Figs. 5 and 6). Almost all crustal profiles are "LVZ-free" in the surrounding areas outside the Plateau, including the western Yangtze Craton, the Tarim Block, the eastern Qilian Block, the Western Yunnan Block, and the Southern Yunnan Block (Fig. 3a). The "LVZ-sharp" type profiles are widely distributed in the hinterland and the eastern marginal area of the Plateau, including the central-eastern Qiangtang Block, the central-eastern Songpan-Ganzi Block, the central-eastern Qaidam Block, the eastern Qilian Block, and the Chuandian Block and its surroundings (black-shaded area in Fig. 3a). The top of those LVZs lies at depths between 15 and 50 km, with relatively large depths > 40 km in the Qiangtang and Lhasa blocks, and relatively small depths < 26 km in the northern and eastern marginal areas of the Plateau (Supplementary Fig. 7). The "LVZ-smooth" type profiles are mainly concentrated in the southeastern marginal area of the Plateau, including the southern Chuandian Block and its southern side, the western Yangtze Craton, and the northern parts of the Western Yunnan and Southern Yunnan blocks (orange-shaded area in Fig. 3a), with sporadic distributions in the northern Chuandian Block, and the eastern Qaidam Block and its surrounding areas.

The LVZs are unlikely to be caused by an elevated temperature alone, a solid-solid composition change or aqueous fluids for the following reasons: (1) an elevated temperature alone cannot explain the sharp velocity discontinuity at the top of LVZs as an elevated temperature would be diffusive across a depth interval due to thermal diffusion; neither can it explain the magnitude of V_S of < 3.40 km s^{-1} in the LVZs as that magnitude of velocity reduction would require an increase of temperature to more than 1000 °C[28,29] enough to induce partial melting; (2) a solid-solid composition change cannot explain the smooth velocity structure in the top of LVZs beneath the southeastern marginal area of the Plateau; neither can it explain the magnitude of V_S of < 3.40 km s^{-1} as the lowest V_S of the known dry metamorphic or plutonic rocks under temperature-pressure conditions in the middle crust of the Plateau (770 °C and 1000 MPa at 30 km depth) is ~3.47 km s^{-1} [28–31]; and (3) aqueous fluids alone cannot explain the magnitude of velocity reductions in the LVZs as petrological studies have suggested that the maximum fluid content would be only around 0.1 percent in the middle-to-lower crust[32,33] insufficient to explain the inferred magnitudes of velocity reduction and inferred magnetotelluric properties in the LVZs (Fig. 1a); aqueous fluids also have a minor effect on V_P/V_S[34] and cannot explain the elevated crustal V_P/V_S values reported in parts of the region[35,36]. The LVZs are thus attributed to be caused by partial melting, as partial melting could explain both the magnitude of V_S and the sharpness of the top velocity structure in the LVZs. Note that the LVZs generally do not extend downward to the Moho discontinuity (Fig. 2 and Supplementary Fig. 4), which may indicate a possible preferential condition for partial melting in the middle crust or a possible metamorphic process at the base of a deep crust[37].

We estimate volume fraction of melt in the LVZs based on the ratio of V_S within the LVZs (V_{S_melt}) over V_S in a melt-free state (V_{S_ref}) and a theoretical relationship between V_{S_melt}/V_{S_ref} and volume fraction of melt derived by Watanabe[34] (Supplementary Note 2 and Supplementary Fig. 8). The estimated maximum melt volume fractions of LVZs lie between 1 and 10 vol%, with 87% of them between 2 and 8 vol%

https://doi.org/10.1038/s41467-025-64607-4

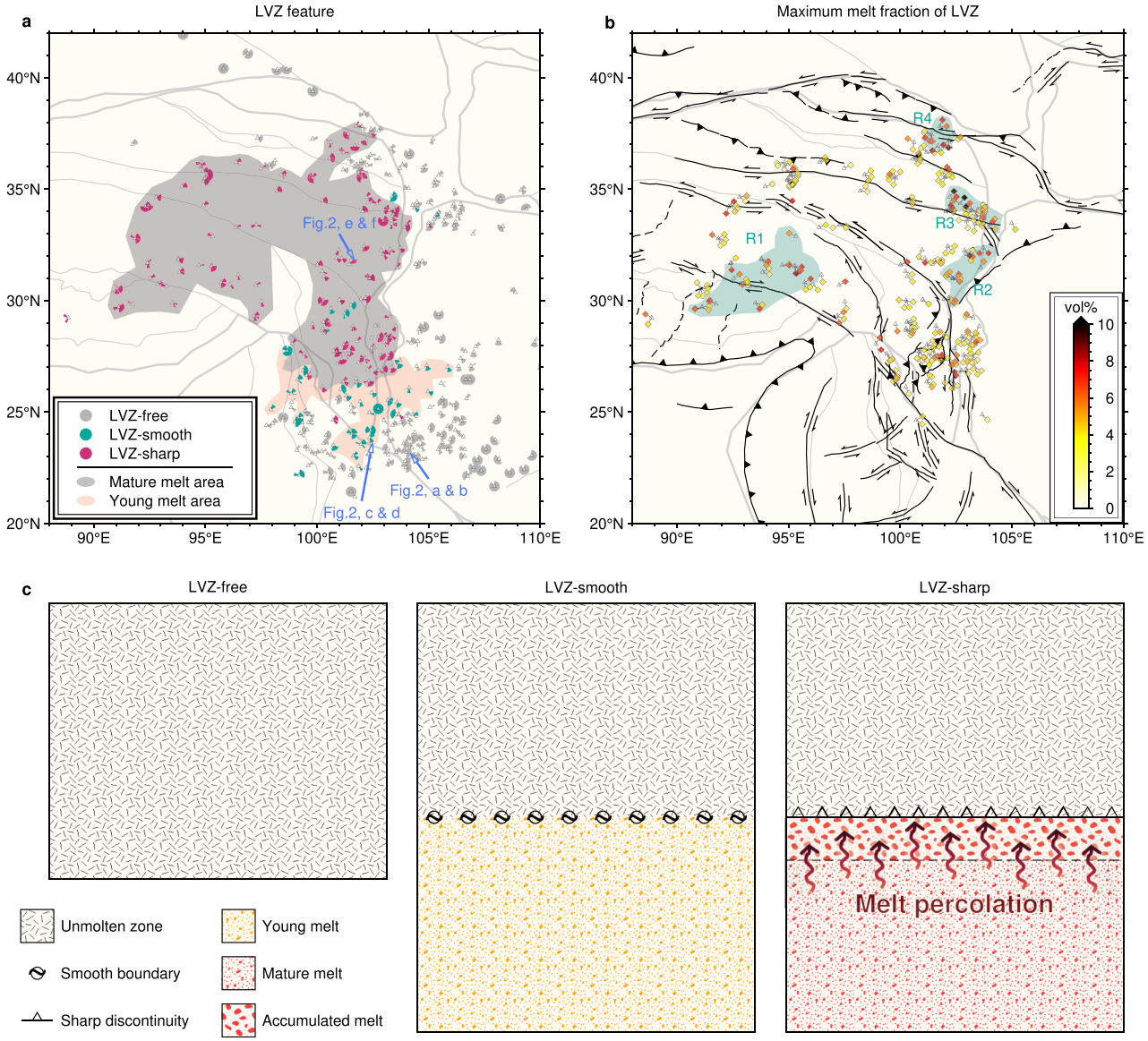

Fig. 3 | Geographic distribution and estimated melt volume fraction of low-velocity zone (LVZ) in the crust. a Geographic distribution of LVZs with a sharp top discontinuity ("LVZ-sharp", magenta sector), LVZs without a sharp top discontinuity ("LVZ-smooth", cyan sector), and no LVZs ("LVZ-free", grey sector). Regions of "LVZ-sharp" and "LVZ-smooth" are marked with a black-shaded area and an orange-shaded area, respectively. Blue arrows point to the example sites of shear-wave velocity (V_S) inversion shown in Fig. 2. **b** Estimated volume fraction of melt for all "LVZ-sharp" sites, with four regions of relatively high values of melt (> 4 vol%) marked with cyan-shaded areas (R1–R4). Major geological faults[49,67] are marked with black lines. (**c**) Interpretation of three types of crustal profiles, with "LVZ-smooth" representing young melt and "LVZ-sharp" representing mature melt that forms a sharp discontinuity in the top after some time of accumulation of melt and enriched composition of decreased solidus.

(Fig. 3b). Four regions are identified to have relatively high values of maximum volume fraction of melt (> 4 vol%): the hinterland of the Qiangtang Block and the eastern area of the Lhasa Block (R1 in Fig. 3b), the eastern Songpan-Ganzi Block adjacent to the western side of the Longmenshan Fault (R2 in Fig. 3b), the vicinities of the East Kunlun Fault including the northeastern Songpan-Ganzi Block and the eastern Qaidam Block (R3 in Fig. 3b), and near the Haiyuan Fault (R4 in Fig. 3b). These regions are located either close to a major fault (R2 to R4), in a region of the thickest crust[35] (R1), or in a region where hot asthenospheric materials were argued to have upwelled following lithospheric delamination during the Triassic (R2)[38,39].

Discussion

The omnipresence of intra-crustal LVZs inside the Plateau, coupled with the absence of intra-crustal LVZs outside the Plateau, suggests that the mid-crustal flow is a major mechanism for the uplift and crustal thickening of the Plateau[6–10]. The inferred magnitude of the fraction of melt could yield a significant decrease in rock viscosity based on the melt-viscosity relationship derived from the laboratory data[40], sufficient to induce a mid-crustal flow based on the numerical models[9,41]. The top discontinuity of the LVZs varies with depth from the hinterland to the marginal areas of the Plateau (Supplementary Fig. 7), possibly reflecting a different degree of shortening of the top layer above the mid-crustal flow channel during the Plateau evolution and/or the existence of lateral variations of thermal and compositional conditions inside the Plateau. The geographic distribution of high-volume melt regions (R1 to R4 in Fig. 3b) also suggests that, besides the radioactive heating in the crust[42], frictional heating of the major faults in the region and a hot underlying mantle are also among the major heat sources of the intra-crustal melts.

Sharpness of the top of LVZ serves as an indicator of the time period of partial melt. Numerical simulations using realistic material properties of the continental crust suggest that melt can migrate through pores in the hot and thick continental crust, with a percolation velocity in the order of millimetres to centimetres per year and a characteristic spacing of 1 mm or larger[43]. Such vertical melt percolation is driven by the density differences between the melt and the surrounding rock and could occur independently of a horizontal advective flow in the middle-to-lower crust. As a result, a certain amount of the percolated melt and an enriched composition of minerals would accumulate at the top of the partial melting zone after some time period of partial melting[43], forming a sharp seismic discontinuity at the top of LVZ. Regions of the "LVZ-sharp" profile are thus regarded as those containing a mature, well-developed, partially molten zone in the middle crust, while regions of the "LVZ-smooth" crustal profile are regarded as those containing a young, less-developed, partially molten zone in the middle crust (Fig. 3c). Based on this classification, the hinterland and eastern marginal area of the Plateau possess mature partially molten zones in the middle crust (termed as "mature melt area", black-shaded area in Fig. 3a) while the southeastern marginal area of the Plateau possesses young partially molten zones in the middle crust (termed as "young melt area", orange-shaded area in Fig. 3a).

Joint analysis of the distribution and characteristics of LVZs, surface topography and the Moho depth (see Supplementary Note 3 and Supplementary Fig. 9 for details on the Moho depth model[24]) reveals three regions of different stages of the Plateau evolution (Fig. 4). The young melt area in the southeastern marginal area of the Plateau is characterized by relatively low surface elevation (averaging 1.98 km, Fig. 4a) and shallow Moho discontinuity (averaging 42.6 km in depth, Supplementary Fig. 9). The mature melt area is marked by two distinct subregions based on the features of surface topography and Moho depth, with the southeastern part of the area having low surface elevation (averaging 2.38 km, Fig. 4a) but deepened Moho discontinuity (averaging 55.0 km in depth, Supplementary Fig. 9), and the remaining region having high surface elevation (averaging 4.01 km, Fig. 4a) and deepened Moho discontinuity (averaging 55.3 km in depth, Supplementary Fig. 9). The topographic difference between the two subregions is unlikely due to a difference of surface erosion between the subregions, as erosion would promote isostatic equilibrium and maintain surface topography in a dynamic Earth[44]; and the topographic difference also indicates an additional contribution of buoyant mid-crustal flow materials within the Plateau in the subregion of high elevation.

These correlations reveal three distinct response stages of the Plateau evolution in response to the mid-crustal flow (Fig. 4b): (1) a pre-response stage when young melts are being developed in the middle-to-lower crust with little uplifting of the surface and little deepening of the Moho discontinuity typified in the region of present-day southern Chuandian Block and its surroundings; (2) the first stage of response of the Plateau by deepening the Moho discontinuity without large-scale surface uplift due to mid-crustal flows in the mature partially molten zone typified in the region of present-day central Chuandian Block and its surroundings; and (3) the last stage of response of the Plateau by large-scale surface uplifting typified in the remaining regions of the present-day Plateau. This last stage of large-scale surface uplifting is also evident in a significantly high uplift rate (1.82 ± 1.51 mm yr^{-1}) observed in the region in comparison with those of the regions in the other two response stages[45–47] (Supplementary Fig. 10).

Our results suggest that the surface responses of the Tibetan Plateau may not necessarily occur in synchrony with the dynamical stages inside the crust. Many types of surface response could occur in a particular stage of the dynamical evolution inside the crust; similar types of surface response could occur in different stages of the dynamical evolution inside the crust; and no surface responses may exist in some stages of the evolution. It should be noted that surface geological processes were extensively studied in the regions of the Plateau, and many evolving stages of the Plateau were proposed based on those geological processes[5,48–50]. Placed in the context of our evolution model, those discoveries suggest that the major geological processes mostly occurred in the region of the last stage of the Plateau evolution, and the surface responded in a complex manner, varying in time and geographic location in this stage. We should also note that while no surface topographic responses yet exist in the pre-response stage and the first stage of the evolution, our model does not preclude other types of surface responses that may or may not be related to these two early stages of the evolution. Our results and those past

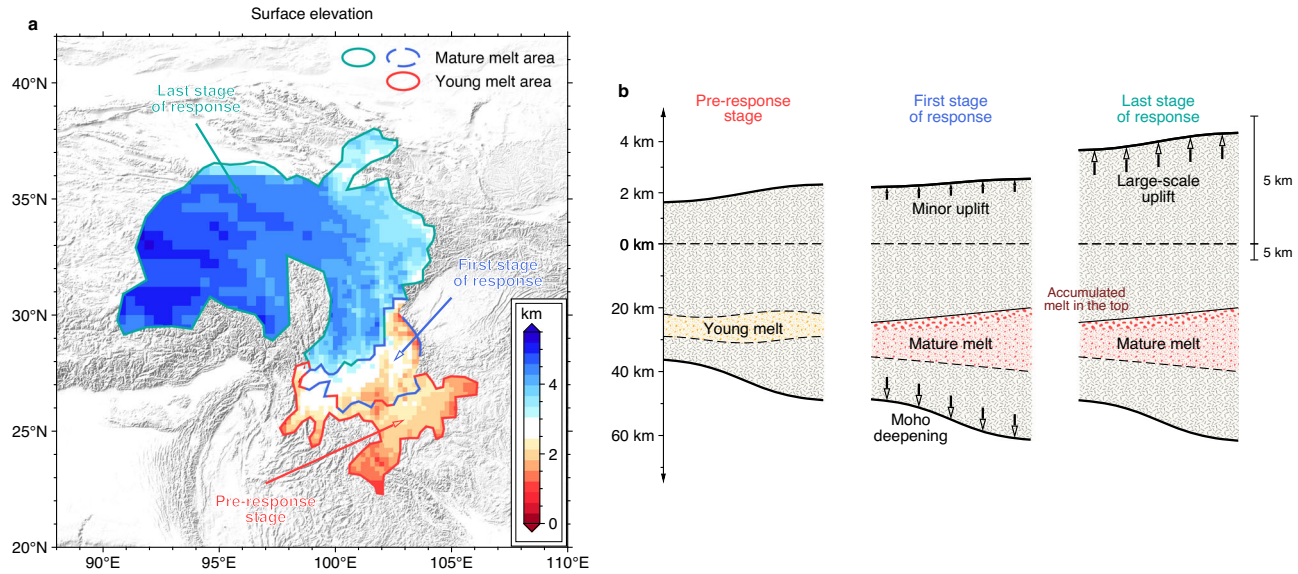

Fig. 4 | Growth stages manifested in the present-day Tibetan Plateau. a Surface elevations (ETOPO1, https://doi.org/10.7289/V5C8276M) in regions of three stages of plateau evolution: pre-response stage (enclosed by red curve), first stage of response (enclosed by blue-dashed curve) and last stage of response (enclosed by cyan curve). **b** Schematic illustration of three stages of plateau evolution: a pre-response stage with a young partially molten zone being developed in the crust, the first stage by deepening the Moho discontinuity with minor uplift at the surface after the maturity of the partially molten zone in the crust, and the last stage by surface uplifting.

discoveries point to the need for future interdisciplinary assimilation of geological and geophysical data in the establishment of a comprehensive dynamical framework for the Plateau evolution.

Our evolution model would provide unique references of continental plateau evolution for future studies of geodynamical mechanism and past plateau evolutions. The geographic distribution, seismic characteristics and dynamic responses of the three evolution stages observed in the present-day Tibetan Plateau would place constraints on future geodynamical models of the Plateau evolution; and the three stages of the Plateau evolution identified in this study would serve as unique references to improve interpretations of the past geological records observed in the Plateau and provide understanding of the past Plateau evolutions. Likely, the inference of the three stages of continental plateau evolution would also be expected to occur in the western region of the Plateau that is currently lacking the seismic coverage and in other collisional orogenic belts worldwide.

Methods

Receiver function (RF) dataset

Teleseismic compressional-wave (*P*-wave) RF dataset is from Cheng et al. [35], which constructed a high-quality RF database from the seismic data recorded at an epicentral distance of 30°–95° in the seismic stations deployed in or around continental China by the China National Seismic Networks (CNSN)[51], the EarthScope and the China Seismic Array (ChinArray) for seismic events with a magnitude ≥ 5.5. High-quality RFs were constructed after the removal of instrument response, a bandpass filter of 0.05–2.00 Hz, a time-domain iterative deconvolution, and a two-step data quality control process[35]. In this study, the RF data within the time window of 1–12 s from the seismic stations within our study region are retained, including a total of 727,201 RFs from 1933 stations (Fig. 1b, 248,092 from 302 CNSN stations, 83,738 from 468 EarthScope stations, and 395,371 from 1,163 ChinArray stations). The time window of 1–12 s is chosen for two reasons: (1) the window is wide enough to contain all *Pms* phases (*P*-to-*S* conversions piercing at the Moho discontinuity), and (2) the RF within the time window of 0–1 s, which is dominated by direct *P*-wave and sedimentary reverberations, has already been fitted in deriving a shallow seismic model of continental China by Xiao et al. [27]; we will adopt it as a priori shallow structure in the joint inversion.

Three pre-processing steps are performed on the RF dataset. Firstly, all RFs in a station are corrected to have the same reference ray parameter of 0.06 s km^{-1} on the basis of the crustal model constructed by Cheng et al. [35]. Secondly, the RFs are stacked based on back-azimuth bins with a bin width of 10°, yielding a total of 60,354 bin-stacked RFs. Finally, noisy bin-stacked RFs are discarded after visual inspection.

We classify the retained bin-stacked RFs into two types based on the presence or absence of a prominent negative phase (i.e., *Pls* phase defined in the text) before the *Pms* phase, yielding 2081 with a prominent *Pls* phase and 2960 without. We further group together similar adjacent bin-stacked RFs that have a correlation coefficient ≥ 0.85 within a back-azimuth range of ≤ 20° into clusters. All bin-stacked RFs in the back-azimuth cluster are further stacked to yield a cluster-stacked RF and the associated uncertainty of the cluster-stacked RF is estimated by calculating the average of the deviations of all raw RFs that contribute to the cluster-stacked RF (the RF uncertainty in the inversion is set to half of the estimated uncertainty by trial and error). Note that we calculate the correlation coefficient for those bin-stacked RFs with a prominent *Pls* phase using the time window of 1 s after the direct *P* phase to 1 s after the *Pls* phase, while for those without that phase using the time window of 1–12 s after the direct *P* phase. We retain only those cluster-stacked RFs that are contributed by more than 10 raw RFs. This clustering procedure yields 324 cluster-stacked RFs with a prominent *Pls* phase and 302 cluster-stacked RFs without that phase.

We illustrate the above RF classification and processing procedures using RFs obtained at station QH.DUL: (1) Raw RFs are obtained from the seismic data of 1011 teleseismic events (Supplementary Fig. 1, a and b); (2) the RFs are corrected to have the same reference ray parameter of 0.06 s km^{-1} and stacked in 36 back-azimuth bins, yielding 9 noisy and 27 high-quality bin-stacked RFs (Supplementary Fig. 1c); (3) the 27 high-quality bin-stacked RFs are classified into two types with 13 having a prominent *Pls* phase and 14 without that phase (Supplementary Fig. 1c); and (4) the high-quality bin-stacked RFs are clustered into 5 similar back-azimuth clusters with 4 having a prominent *Pls* phase and 1 without that phase, along with associated uncertainties estimated (Supplementary Fig. 1c and d).

In this study, we aim to determine crustal low-velocity zone (LVZ) structure beneath seismic stations in different back-azimuth ranges, as the distribution and features of the partially molten zones could vary on a small geographic scale. The azimuthal difference in RFs could also be the result of seismic anisotropy or a dipping seismic structure, and a harmonic stripping method[52] is usually applied to extract or remove those related signals. In the present case, as the RF signals are dominated by the conversions from the top of the LVZs and our goal is to detect fine structures of LVZs, we adopt the RF azimuth-clustering analysis without applying the harmonic stripping method. The application of harmonic stripping could remove signals associated with seismic anisotropy or a dipping seismic structure, but it would also remove signals that are dominated by lateral variations of LVZs.

Rayleigh wave phase velocity dataset

The Rayleigh wave phase velocity models (Supplementary Fig. 2a) are inverted based on a Rayleigh wave phase velocity dataset constructed from data sources of seismic stations and seismic events in or around continental China (Supplementary Fig. 2, b and c). The Rayleigh wave phase velocity dataset is constructed based on phase velocity dispersion curves measured between 639,171 inter-station and 54,792 event-station pairs.

The inter-station phase velocity dispersion curves are measured based on continuous seismic ambient noise recorded on vertical components of 4435 seismic stations, spanning a period range of 8–50 s. The 4435 seismic stations are deployed in or around continental China (Supplementary Fig. 2b), including (1) 1120 permanent stations of the China National Seismic Networks (CNSN)[51] from 2015 to 2017, (2) 1770 temporary stations of the China Seismic Array (ChinArray) from 2006 to 2016, (3) 81 temporary seismic stations of the Seismic Array iNtegrated Detection for a Window of Indian Continental Head (SANDWICH) from 2013 to 2017, (4) 71 temporary stations of the Middle-Lower Yangtze broadband seismic Network (MLYN) from 2012 to 2016, and (5) 1393 temporary stations from 1991 to 2020 with data downloaded from the Public seismic Data Management Centers (PDMC) of the EarthScope, the GFZ German Research Centre for Geosciences (GEOFON), the Swiss Seismological Service (SED), and the French seismological and geodetic network Resif-Epos (RESIF). We first follow the ambient noise data processing procedure described by Xiao et al. [25] to compute the inter-station empirical Green's functions (EGFs) of each station pair. We down-sample the waveform data to 1 Hz, remove the instrument response from the data, apply a bandpass filter of 0.008–0.3 Hz to the data, cut the continuous waveform data into daily segments, perform temporal normalization and spectrum whitening for the daily waveform segments[53,54], calculate the cross-correlation function of the pre-processed daily waveform segments, stack the daily cross-correlation functions in one year, and calculate an inter-station empirical Green's function (EGF) by averaging the causal and acausal parts of the stack. We then measure the inter-station Rayleigh wave phase dispersion curves from the inter-station EGFs by applying a frequency-time analysis technique[55,56].

The event-station phase velocity dispersion curves are measured based on Rayleigh wave waveform data of 226 intermediate

earthquakes recorded on vertical components of 1463 seismic stations, spanning a period range of 8–70 s. The 1463 seismic stations are from the CNSN, SANDWICH, MLYN, and PDMC, and the 226 intermediate earthquakes occurred from 2012 to 2019 in or around western China with a magnitude range 4.5 ≤ Mw ≤ 7.0 based on the catalogue from the Global Centroid Moment Tensor (GCMT) project[57] (Supplementary Fig. 2c). We first follow the procedures described by Xiao et al. [25] to preprocess the Rayleigh wave waveform data. We isolate the Rayleigh wave waveforms from the seismic records based on a group velocity range of 1.5–4.5 km s^{-1}, down-sample the waveform data to 1 Hz, remove the instrument response from the data, rotate the horizontal components to the radial component along the great circle plane, and apply a bandpass filter of 0.008–0.3 Hz to the data. We then estimate event-station Rayleigh wave phase velocity dispersion curves from the preprocessed waveform data by adopting a time-domain waveform matching algorithm[58,59]. The algorithm constructs a composite synthetic Rayleigh wave waveform by perturbing the phase velocity dispersion and spectral amplitudes of a reference synthetic Rayleigh wave waveform. The phase velocity dispersion and spectral amplitudes that yield the best fit between the composite synthetic waveform and the observed waveform are considered to be the optimal measurements.

The inter- and event-station Rayleigh wave phase velocity measurements are quality-controlled following the procedures described by Xiao et al. [25]. For each period, we discard those inter- and event-station phase velocity measurements with an epicentral distance smaller than two wavelengths, a deviation from the average phase velocity larger than 20%, and a travel time residual from the predicted travel time based on the model of Shen et al. [60] larger than 20 s. We also discard those inter-station phase velocity measurements with a signal-to-noise ratio of EGF (i.e., the ratio of the maximum amplitude in the windowed Rayleigh wave signal over the standard deviation of amplitudes in the windowed seismic ambient noise) smaller than 5, and those event-station phase velocity measurements with a signal ratio (i.e., the spectral amplitude ratio of the undispersed Rayleigh wave waveform over the original waveform) smaller than 0.6, a waveform misfit (i.e., the waveform difference between the composite synthetic and observed Rayleigh wave waveforms) larger than 0.3, a total number of measurements per earthquake smaller than 30, and an azimuthal variation of phase travel time residuals of an earthquake larger than 10 s.

The Rayleigh wave phase velocity models (Supplementary Fig. 2a) are then inverted by applying a simultaneous inversion method[25], with models in the period range of 8–50 s constrained by both the inter- and event-station measurements and those in the period range of 50–70 s solely constrained by the event-station measurements. We first invert a preliminary Rayleigh wave phase velocity structure based on the inter-station phase velocity measurements. We then redetermine centroid depths and scalar moments of 226 intermediate earthquakes based on the observed Rayleigh and Love wave spectral amplitudes, relocate centroid parameters of geographic location and origin time of those earthquakes based on the event-station Rayleigh wave phase velocity measurements and the preliminary Rayleigh wave phase velocity structure obtained in the first step, and update the event-station Rayleigh wave phase velocity measurements based on the relocated centroid geographic locations and origin times. We finally invert a final Rayleigh wave phase velocity model and construct a set of earthquake centroid geographic locations and origin times based on the inter- and event-station phase velocity measurements. We estimate the uncertainty of the inferred Rayleigh wave phase velocity with a Monte Carlo error propagation technique based on the unexplained travel time residuals after simultaneous inversion[25,61]. In this study, the inverted phase velocity models and associated uncertainties are collected for 346 stations that have high-quality RFs.

Rayleigh wave ZH ratio dataset

The Rayleigh wave vertical/horizontal (ZH) displacement ratio dataset is constructed for 346 seismic stations that have high-quality RFs, from 4709 seismic events sampling the region with a magnitude > 5.5, an event depth < 60 km, and an epicentral distance range of 20°–140° (Fig. 1b and Supplementary Fig. 3). In this study, high-quality Rayleigh wave ZH ratios are measured in the period range of 20–80 s following procedures described by Tanimoto and Rivera[62]. We isolate the Rayleigh wave waveforms from the seismic records based on a group velocity range of 1.5–4.5 km s^{-1}, down-sample the three-component waveform data to 1 Hz, remove the instrument response from the data, apply a bandpass filter of 0.008–0.3 Hz to the data, and rotate the horizontal components to the radial component along the event-station great circle plane. We apply a series of narrowband Gaussian filters with central frequencies varying from 20 to 80 s to the preprocessed waveform data and perform the Hilbert transform on the vertical component to correct for the 90° phase shift between the vertical and radial components of the Rayleigh wave. For each station, a ZH ratio is first calculated for each Rayleigh wave observation by dividing the maximum amplitude of the envelope of its phase-advanced vertical component over that of the envelope of its radial component. Those ZH ratio measurements are discarded: (1) the cross-correlation coefficient between the waveforms of the radial and phase-advanced vertical components smaller than 0.7, (2) the signal-to-noise ratio (i.e., the ratio of the maximum amplitude in the windowed Rayleigh wave signal over the standard deviation of amplitudes in the windowed seismic ambient noise) smaller than 8, (3) the total number of measurements at the period smaller than 15, (4) the abnormal value outside the range of 0.4–2, and (5) the deviation from the average ZH ratio larger than two standard deviations of all measurements. The mean and three standard deviations of all quality-controlled individual ZH ratio measurements associated with the observations of the seismic station are taken as the ZH ratio measurement and associated uncertainty of the station, respectively. Uncertainties smaller than 4% of the ZH ratio measurement are set to 4% of the measurement.

Joint inversion scheme and model parametrization

We adopt the joint inversion method developed by Xiao et al. [27] to constrain one-dimensional seismic structures below a seismic station in various back-azimuth clusters. Along a certain back-azimuth cluster, the joint inversion uses the cluster-stacked RF along the back-azimuth cluster and the dispersion curves of phase velocity and ZH ratio. The inversion process uses a Markov Chain Monte Carlo algorithm[26,27] to search for the V_S model that best fits the RF and dispersion curves of phase velocity and ZH ratio by minimizing an objective function defined as:

$$S_{\text{joint}}(m) = \alpha S_{\text{RF}}(\text{m}) + \beta S_{\text{PV}}(\text{m}) + \gamma S_{\text{ZH}}(m) + \omega S_{\text{SM}}(m) \tag{1}$$

and

$$S_{\text{SM}} = \frac{1}{N-1}\sum_{i=1}^{N-1} \frac{H(V_i - V_{i+1})\,||(V_i - V_{i+1})||}{0.01 \cdot (d_{i+1} - d_i)} \cdot \varphi(d_i) \tag{2}$$

$$H(n) = \begin{cases} 0 & n \le 0 \\ 1 & n > 0 \end{cases} \tag{3}$$

$$\varphi(d_i) = \begin{cases} 0 & 10 \le d_i \le (d_{\text{m}} - 10) \\ 1 & d_i < 10 \text{ or } d_i > (d_{\text{m}} - 10) \end{cases} \tag{4}$$

Where S_{RF}, S_{PV} and S_{ZH} are the mean values of the squares of the L2-norm misfits between observations and synthetics over all time or period sampling points for three types of seismic data, weighted by

uncertainties of the data respectively. In practice, the RF uncertainties are set to the median of the uncertainties within the RF time window of 0–15 s; and the phase velocity uncertainties are amplified by a factor of 2.8 by trial and error. S_{SM} is the model smoothness term that penalizes presence of local low-velocity zones at the depth shallower than 10 km or deeper than $(d_m - 10)$ km (d_m is the Moho depth) with 0.01 s^{-1} for normalization. V_i and d_i are V_S of the i th discretized sublayer (N sublayers in total) and its depth to the surface respectively. Relative weighting parameters between the RF misfit (α), phase velocity misfit (β), ZH ratio misfit (γ) and model smoothness term (ω) are set to 1, 1, 1 and 1 (with an absolute value of 40) by trial and error. In practice, the V_S model and its uncertainty are estimated through statistical analysis of the model assemblage selected from sampled models in 50,000 iterations after the first 200 iterations of the burn-in phase. The best-fitting V_S model is defined as the sampled model nearest to the average of all acceptable models and the model uncertainty is defined as two standard deviations of all acceptable models. The model assemblage is constructed by selecting models with a small value of a normalized objective function defined as:

$$\varepsilon_{norm}(m) = \left(\frac{S_{RF}(m)}{S_{RF}(m_{rf})} + \frac{S_{PV}(m)}{S_{PV}(m_{pv})} + \frac{S_{ZH}(m)}{S_{ZH}(m_{zh})} + \frac{S_{SM}(m)}{S_{SM}(m_{sm})}\right)/4 \quad (5)$$

where sampled models with the minimal RF misfit ($S_{RF}(m_{rf})$), the minimal phase velocity misfit ($S_{PV}(m_{pv})$), the minimal ZH ratio misfit ($S_{ZH}(m_{zh})$), and the minimal model smoothness ($S_{SM}(m_{sm})$) are employed for normalization. The model assemblage consists of the models with a normalized objective function value smaller than ($\varepsilon_{norm}(m_{all}) + 2$), where m_{all} is the sampled model with the minimum value of the objective function.

Two separate model parametrization schemes are used in accordance with the presence or absence of *Pls* phase in the cluster-stacked RF. For the observations with the cluster-stacked RF exhibiting no *Pls* phase, V_S profile is parameterized with three layers: a shallow sediment, a crystalline crust and an uppermost mantle. The V_S profile and thickness of the sediment layer are adopted from Xiao et al. [27], while the V_S profiles in the crystalline crust and the uppermost mantle are represented by a combination of B-spline functions with seven independent parameters for the crystalline crust layer and five for the uppermost mantle layer. The seven parameters for the crystalline crust layer include the thickness of the layer and coefficients of six B-spline functions used to represent the velocity structure inside the layer, while the five parameters for the uppermost mantle layer are coefficients of five B-spline functions used to represent the velocity structure in the uppermost mantle. For the observations with the cluster-stacked RF exhibiting a prominent *Pls* phase, a low-velocity zone (LVZ) is added in the crystalline crust layer. The LVZ is represented by a top sharp discontinuity and a velocity decrease followed by a linear gradient of increasing V_S toward the bottom, and is parameterized with three free parameters, including the depth of the top boundary of the LVZ, V_S decrease across the top boundary and thickness of the LVZ. The V_S jump across the bottom boundary of the LVZ is set to zero, as we do not observe a corresponding positive phase in all the RFs. The depth of the top boundary is allowed to vary over a depth span of 40 km, centred on an initial depth calculated based on the arrival time of the *Pls* phase and a velocity model[60], while the thickness of the LVZ is restricted to being in a range of 0–30 km and the velocity reduction across the top boundary is required to be less than 1.0 km s^{-1}.

Initial models are constructed based on a priori information from several previous studies, with shallow V_S structure adopted from Xiao et al. [27], crustal thickness and V_P/V_S values from Cheng et al. [35], V_P structure in the uppermost mantle from Ma et al. [63], and V_S structure in the crystalline crust from Shen et al. [60]. V_P are inferred from V_S based on the empirical relationship proposed by Brocher[64] in the regions of no coverage of crustal V_P/V_S values.

Data availability

The raw and cluster-stacked receiver functions, phase velocities and ZH ratios of the Rayleigh wave used in the joint inversion and the inverted seismic models generated in this study have been deposited in Zenodo[65] (https://doi.org/10.5281/zenodo.15873825). The inter-station empirical Green's functions, event-station Rayleigh wave phase velocity dispersion curves, Rayleigh wave phase velocity maps and the crustal thickness model of CSRM-1.0 that support the findings of this study are available in Zenodo[66] (https://doi.org/10.5281/zenodo.8103561). The seismic waveforms recorded by permanent stations in CNSN are provided by the China Earthquake Networks Center and AH, BJ, BU, CQ, FJ, GD, GS, GX, GZ, HA, HB, HE, HI, HL, HN, JL, JS, JX, LN, NM, NX, QH, SC, SD, SH, SN, SX, TJ, XJ, XZ, YN, ZJ Seismic Networks, China Earthquake Administration and distributed by the China Seismological Reference Model (http://chinageorefmodel.org/) Product Center (https://data.earthquake.cn/ in Chinese and http://chinageorefmodel.org/data/level1 in English). The seismic waveforms recorded by temporary stations in ChinArray are provided by the China Seismic Array Data Management Center at Institute of Geophysics, China Earthquake Administration (https://doi.org/10.17616/R31NJMMK). The waveforms of temporary stations in SANDWICH are provided by the Seismic Array Laboratory, Institute of Geology and Geophysics, Chinese Academy of Sciences (http://chinageorefmodel.org/data/level1). The seismic waveforms of temporary stations in MLYN are provided by the China Deep Exploration Center, Chinese Academy of Geological Sciences (http://chinageorefmodel.org/data/level1). These waveforms are accessible from these data centers following their respective regulations. The waveform data of temporary stations in PDMC are downloaded from four Public Data Management Centers of the EarthScope Data Services (https://ds.iris.edu/ds/), the GFZ German Research Centre for Geosciences (https://geofon.gfz-potsdam.de/), the Swiss Seismological Service (http://seismo.ethz.ch/en/home/) and the French seismological and geodetic network Resif-Epos (https://seismology.resif.fr/).Correspondence and requests for materials should be addressed to Lianxing Wen. Source data are provided with this paper.

Code availability

The inversion codes that support the findings of this study are available in Zenodo[65] (https://doi.org/10.5281/zenodo.15873825).

References

1. England, P. & Houseman, G. Finite strain calculations of continental deformation: 2. Comparison with the India-Asia Collision Zone. *J. Geophys. Res.: Solid Earth* **91**, 3664–3676 (1986).
2. England, P. & Molnar, P. Active Deformation of Asia: From Kinematics to Dynamics. *Science* **278**, 647–650 (1997).
3. Molnar, P. & Tapponnier, P. Cenozoic Tectonics of Asia: Effects of a Continental Collision. *Science* **189**, 419–426 (1975).
4. Avouac, J. & Tapponnier, P. Kinematic model of active deformation in central Asia. *Geophys Res Lett.* **20**, 895–898 (1993).
5. Tapponnier, P. et al. Oblique Stepwise Rise and Growth of the Tibet Plateau. *Science* **294**, 1671–1677 (2001).
6. Bird, P. Lateral extrusion of lower crust from under high topography in the isostatic limit. *J. Geophys. Res.: Solid Earth* **96**, 10275–10286 (1991).
7. Royden, L. H. Coupling and decoupling of crust and mantle in convergent orogens: Implications for strain partitioning in the crust. *J. Geophys. Res.: Solid Earth* **101**, 17679–17705 (1996).
8. Royden, L. H. et al. Surface deformation and lower crustal flow in Eastern Tibet. *Science* **276**, 788–790 (1997).
9. Clark, M. K. & Royden, L. H. Topographic ooze: Building the eastern margin of Tibet by lower crustal flow. *Geology* **28**, 703–706 (2000).
10. Beaumont, C., Jamieson, R. A., Nguyen, M. H. & Lee, B. Himalayan tectonics explained by extrusion of a low-viscosity crustal channel coupled to focused surface denudation. *Nature* **414**, 738–742 (2001).

11. Shen, F., Royden, L. H. & Burchfiel, B. C. Large-scale crustal deformation of the Tibetan Plateau. *J. Geophys. Res.: Solid Earth* **106**, 6793–6816 (2001).
12. Wang, C. et al. Constraints on the early uplift history of the Tibetan Plateau. *Proc. Natl. Acad. Sci.* **105**, 4987–4992 (2008).
13. Wang, E. et al. Two-phase growth of high topography in eastern Tibet during the Cenozoic. *Nat. Geosci.* **5**, 640–645 (2012).
14. Ding, L. et al. Timing and mechanisms of Tibetan Plateau uplift. *Nat. Rev. Earth Environ.* **3**, 652–667 (2022).
15. Kind, R. et al. Evidence from earthquake data for a partially molten crustal layer in Southern Tibet. *Science* **274**, 1692–1694 (1996).
16. Li, H., Su, W., Wang, C. & Huang, Z. Ambient noise Rayleigh wave tomography in western Sichuan and eastern Tibet. *Earth Planet Sc. Lett.* **282**, 201–211 (2009).
17. Yao, H., van der Hilst, R. D. & Montagner, J. Heterogeneity and anisotropy of the lithosphere of SE Tibet from surface wave array tomography. *J. Geophys. Res.: Solid Earth* **115** (2010). https://doi.org/10.1029/2009JB007142
18. Yang, Y. et al. A synoptic view of the distribution and connectivity of the mid-crustal low velocity zone beneath Tibet. *J. Geophys. Res.: Solid Earth* **117** (2012). https://doi.org/10.1029/2011JB008810
19. Li, H. et al. The distribution of the mid-to-lower crustal low-velocity zone beneath the northeastern Tibetan Plateau revealed from ambient noise tomography. *J. Geophys. Res.: Solid Earth* **119**, 1954–1970 (2014).
20. Liu, Q. et al. Eastward expansion of the Tibetan Plateau by crustal flow and strain partitioning across faults. *Nat. Geosci.* **7**, 361–365 (2014).
21. Bao, X. et al. Two crustal low-velocity channels beneath SE Tibet revealed by joint inversion of Rayleigh wave dispersion and receiver functions. *Earth Planet Sc. Lett.* **415**, 16–24 (2015).
22. Deng, Y., Li, J., Song, X. & Zhu, L. Joint inversion for lithospheric structures: implications for the growth and deformation in Northeastern Tibetan Plateau. *Geophys Res Lett.* **45**, 3951–3958 (2018).
23. Wen, L. & Yu, S. The China Seismological Reference Model project. *Earth Planet. Phys.* **7**, 521–532 (2023).
24. Xiao, X. et al. CSRM-1.0: A China Seismological Reference Model. *J. Geophys. Res.: Solid Earth* **129**, e2024JB029520 (2024).
25. Xiao, X., Sun, L., Wang, X. & Wen, L. Simultaneous Inversion for Surface Wave Phase Velocity and Earthquake Centroid Parameters: Methodology and Application. *J. Geophys. Res.: Solid Earth* **127**, e2022JB024018 (2022).
26. Sambridge, M. Geophysical inversion with a neighbourhood algorithm—I. Searching a parameter space. *Geophys J. Int* **138**, 479–494 (1999).
27. Xiao, X. et al. Shallow seismic structure beneath the continental China revealed by P-wave polarization, Rayleigh wave ellipticity and receiver function. *Geophys J. Int* **225**, 998–1019 (2021).
28. Christensen, N. I. Poisson's ratio and crustal seismology. *J. Geophys. Res.: Solid Earth* **101**, 3139–3156 (1996).
29. Kern, H. et al. Pressure and temperature dependence of VP and VS in rocks from the superdeep well and from surface analogues at Kola and the nature of velocity anisotropy. *Tectonophysics* **338**, 113–134 (2001).
30. Agius, M. R. & Lebedev, S. Shear-velocity structure, radial anisotropy and dynamics of the Tibetan crust. *Geophys J. Int.* **199**, 1395–1415 (2014).
31. Hacker, B. R., Ritzwoller, M. H. & Xie, J. Partially melted, mica-bearing crust in Central Tibet. *Tectonics* **33**, 1408–1424 (2014).
32. Li, S. et al. Partial melt or aqueous fluid in the mid-crust of Southern Tibet? Constraints from INDEPTH magnetotelluric data. *Geophys J. Int* **153**, 289–304 (2003).
33. Yardley, B. W. D. & Valley, J. W. The petrologic case for a dry lower crust. *J. Geophys. Res.: Solid Earth* **102**, 12173–12185 (1997).
34. Watanabe, T. Effects of water and melt on seismic velocities and their application to characterization of seismic reflectors. *Geophys Res Lett.* **20**, 2933–2936 (1993).
35. Cheng, S. et al. Crustal thickness and Vp/Vs variation beneath continental China revealed by receiver function analysis. *Geophys J. Int* **228**, 1731–1749 (2021).
36. Xin, H. et al. Three-Dimensional Lithospheric VP/VS Structure Beneath Chinese Continent. *Seismol. Res. Lett.* (2024). https://doi.org/10.1785/0220240015
37. Tang, M., Chen, H., Lee, C.-T. A. & Cao, W. Subaerial crust emergence hindered by phase-driven lower crust densification on early Earth. *Sci. Adv.* **10**, eadq1952 (2024).
38. Zhang, H. et al. A-type granite and adakitic magmatism association in Songpan–Garze fold belt, eastern Tibetan Plateau: Implication for lithospheric delamination. *Lithos* **97**, 323–335 (2007).
39. Yuan, C. et al. Triassic granitoids in the eastern Songpan Ganzi Fold Belt, SW China: Magmatic response to geodynamics of the deep lithosphere. *Earth Planet Sc. Lett.* **290**, 481–492 (2010).
40. Rosenberg, C. L. & Handy, M. R. Experimental deformation of partially melted granite revisited: implications for the continental crust. *J. Metamorph. Geol.* **23**, 19–28 (2005).
41. Beaumont, C., Jamieson, R. A., Nguyen, M. H. & Medvedev, S. Crustal channel flows: 1. Numerical models with applications to the tectonics of the Himalayan-Tibetan orogen. *J. Geophys. Res.: Solid Earth* **109** (2004).
42. Henry, P., Le Pichon, X. & Goffé, B. Kinematic, thermal and petrological model of the Himalayas: constraints related to metamorphism within the underthrust indian crust and topographic elevation. *Tectonophysics* **273**, 31–56 (1997).
43. Maierová, P., Hasalová, P., Schulmann, K., Štípská, P. & Souček, O. Porous Melt Flow in Continental Crust—A Numerical Modeling Study. *J. Geophys. Res.: Solid Earth* **128**, e2023JB026523 (2023).
44. Avouac, J. P. & Burov, E. B. Erosion as a driving mechanism of intracontinental mountain growth. *J. Geophys. Res.: Solid Earth* **101**, 17747–17769 (1996).
45. Liang, S. et al. Three-dimensional velocity field of present-day crustal motion of the Tibetan Plateau derived from GPS measurements. *J. Geophys. Res.: Solid Earth* **118**, 5722–5732 (2013).
46. Hao, M., Freymueller, J. T., Wang, Q., Cui, D. & Qin, S. Vertical crustal movement around the southeastern Tibetan Plateau constrained by GPS and GRACE data. *Earth Planet Sc. Lett.* **437**, 1–8 (2016).
47. Pan, Y., Shen, W.-B., Shum, C. K. & Chen, R. Spatially varying surface seasonal oscillations and 3-D crustal deformation of the Tibetan Plateau derived from GPS and GRACE data. *Earth Planet Sc. Lett.* **502**, 12–22 (2018).
48. Cao, K. et al. Oligocene-Early Miocene Topographic Relief Generation of Southeastern Tibet Triggered by Thrusting. *Tectonics* **38**, 374–391 (2019).
49. Pitard, P. et al. Exhumation History Along the Muli Thrust—Implication for Crustal Thickening Mechanism in Eastern Tibet. *Geophys Res Lett.* **48**, e2021GL093677 (2021).
50. Zhang, G. et al. Progressive tectonic evolution from crustal shortening to mid-lower crustal expansion in the southeast Tibetan Plateau: A synthesis of structural and thermochronological insights. *Earth-Sci. Rev.* **226**, 103951 (2022).
51. Zheng, X., Yao, Z., Liang, J. & Zheng, J. The role played and opportunities provided by IGP DMC of China National Seismic Network in Wenchuan Earthquake Disaster Relief and Researches. *B Seismol Soc. Am.* **100**, 2866–2872 (2010).
52. Shen, W., Ritzwoller, M. H., Schulte-Pelkum, V. & Lin, F.-C. Joint inversion of surface wave dispersion and receiver functions: a Bayesian Monte-Carlo approach. *Geophys J. Int.* **192**, 807–836 (2012).
53. Bensen, G. D. et al. Processing seismic ambient noise data to obtain reliable broad-band surface wave dispersion measurements. *Geophys J. Int* **169**, 1239–1260 (2007).

54. Goutorbe, B., de Oliveira Coelho, D. L. & Drouet, S. Rayleigh wave group velocities at periods of 6–23 s across Brazil from ambient noise tomography. *Geophys J. Int* **203**, 869–882 (2015).
55. Levshin, A. L., Pisarenko, V. F. & Pogrebinsky, G. A. On a frequency-time analysis of oscillations. *Ann. Géophys.* **28**, 211–218 (1972).
56. Levshin, A. L. & Ritzwoller, M. H. in *Monitoring the Comprehensive Nuclear-Test-Ban Treaty: Surface Waves* (eds Anatoli L. Levshin & Michael H. Ritzwoller) 1531-1545 (Birkhäuser Basel, 2001).
57. Ekström, G., Nettles, M. & Dziewoński, A. M. The global CMT project 2004–2010: Centroid-moment tensors for 13,017 earthquakes. *Phys. Earth Planet* **200-201**,1–9(2012).
58. Ekström, G., Tromp, J. & Larson, E. W. F. Measurements and global models of surface wave propagation. *J. Geophys. Res.: Solid Earth* **102**, 8137–8157 (1997).
59. Ekström, G. A global model of Love and Rayleigh surface wave dispersion and anisotropy, 25-250 s. *Geophys J. Int* **187**, 1668–1686 (2011).
60. Shen, W. et al. A seismic reference model for the crust and uppermost mantle beneath China from surface wave dispersion. *Geophys J. Int* **206**, 954–979 (2016).
61. Aster, R., Borchers, B. & Thurber, C. in *Parameter Estimation and Inverse Problems (Third Edition)* (eds Richard C. Aster, Brian Borchers, & Clifford H. Thurber) ix-xi (Elsevier, 2019).
62. Tanimoto, T. & Rivera, L. The ZH ratio method for long-period seismic data: sensitivity kernels and observational techniques. *Geophys. J. Int* **172**, 187–198 (2008).
63. Ma, J. et al. Uppermost Mantle Seismic Pn-Velocity in Continental China and Its Tectonic Implications. *J. Geophys. Res.: Solid Earth* **128**, e2022JB025667 (2023).
64. Brocher, T. M. Empirical relations between elastic wavespeeds and density in the Earth's Crust. *B Seismol Soc. Am.* **95**, 2081–2092 (2005).
65. Cheng, S. et al. A dataset related to the manuscript entitled "Three evolution stages of continental plateau manifested in the present-day Tibetan Plateau" [Data set]. *Zenodo*. https://doi.org/10.5281/zenodo.15873825 (2025).
66. Group, C. S. R. M. C. China Seismological Reference Model (CSRM) - Models and Datasets [Data set]. *Zenodo*. https://doi.org/10.5281/zenodo.8103561 (2023).
67. Yin, A. & Harrison, T. M. Geologic evolution of the Himalayan-Tibetan Orogen. *Annu Rev. Earth Pl Sc.* **28**, 211–280 (2000).
68. Zhang, P. et al. Active tectonic blocks and strong earthquakes in the continent of China. *Sci. China Ser. D: Earth Sci.* **46**, 13–24 (2003).

Acknowledgements

We are grateful to the colleagues in the China Earthquake Administration and other related institutions on the deployment and operation of the seismic stations, and the China Seismological Reference Model Project for its efforts in collecting and sharing the seismic data (http://chinageorefmodel.org/). This study is supported by the National Natural Science Foundation of China (under grants NSFC42250201 and NSFC42130301 received by L.W.) and the Fundamental Research Funds for the Central Universities (under grant WK2080000197 received by S.C.).

Author contributions

L.W. contributed to project conceptualization and project supervision; S.C., X.X. and L.W. contributed to methodology, software, data curation and preparation of the original draft; L.S., W.W., J.W., X.W., X.L., X.T., H.L. and L.W. contributed to seismic waveform data acquisition; S.C. and L.W. contributed to funding acquisition, formal analysis and visualization; All authors contributed to review and editing of the paper.

Competing interests

The authors declare no competing interests.

Additional information

Supplementary information The online version contains supplementary material available at https://doi.org/10.1038/s41467-025-64607-4.

Correspondence and requests for materials should be addressed to Lianxing Wen.

Peer review information *Nature Communications* thanks Stéphane Guillot, Anne Replumaz, Leigh (Wiki) Royden, and the other, anonymous, reviewer(s) for their contribution to the peer review of this work. A peer review file is available.

Reprints and permissions information is available at http://www.nature.com/reprints

Publisher's note Springer Nature remains neutral with regard to jurisdictional claims in published maps and institutional affiliations.

Open Access This article is licensed under a Creative Commons Attribution-NonCommercial-NoDerivatives 4.0 International License, which permits any non-commercial use, sharing, distribution and reproduction in any medium or format, as long as you give appropriate credit to the original author(s) and the source, provide a link to the Creative Commons licence, and indicate if you modified the licensed material. You do not have permission under this licence to share adapted material derived from this article or parts of it. The images or other third party material in this article are included in the article's Creative Commons licence, unless indicated otherwise in a credit line to the material. If material is not included in the article's Creative Commons licence and your intended use is not permitted by statutory regulation or exceeds the permitted use, you will need to obtain permission directly from the copyright holder. To view a copy of this licence, visit http://creativecommons.org/licenses/by-nc-nd/4.0/.

© The Author(s) 2025